https://doi.org/10.5194/egusphere-2025-4746
Preprint. Discussion started: 21 October 2025

Impacts of orography and urbanization on extreme precipitation event in Beijing during 2023

Haobo Cui[1], Hongyong Yu[1], Xingshuo Zuo[1] and Guocan Wu[1*]

[1]State Key Laboratory of Earth Surface Processes and Disaster Risk Reduction, Faculty of Geographical Science, Beijing Normal University, Beijing, 100875 China

[*]*Corresponding author*: Guocan Wu

E-mail address: gcwu@bnu.edu.cn

https://doi.org/10.5194/egusphere-2025-4746
Preprint. Discussion started: 21 October 2025

Abstract

The effects of urbanization and topographic uplift play significant roles in extreme precipitation events, and therefore in water management. In this study, we analyzed main impact factors in an extreme precipitation event that occurred during July 2023 in Beijing, using the Weather Research and Forecasting (WRF) model. The results showed that the main cause of this precipitation event was the residual forces of Typhoon Doksuri combined with water vapor transported from the subtropical high. The orographic effect altered the spatial pattern of accumulated precipitation throughout the simulation period by changing the local circulation, as the accumulated precipitation in the southwestern mountainous regions increased by 229.42 mm (41.34%), and the precipitation in the plain areas decreased by 83.59 mm (43.50%). The impact of the underlying urban surface led to accumulated precipitation in the southwestern mountainous regions of Beijing decreasing by 88.07 mm (15.87%). Further analysis showed that topographical features caused the uplift of air masses in the mountainous regions and prevented the low-pressure system propagate northward, leading to significant enhancement of the convective intensity over Beijing and precipitation for a prolonged duration. The presence of urban surfaces contributed to reductions in the latent heat flux and wind speed, resulting in decreased energy transfer to the southwestern mountainous regions via easterly winds. This reduction in energy suppressed convective activity and subsequently led to a decrease in precipitation in these regions. As extreme precipitation events become more frequent, the comprehensive research into such events may help with prevention and the response to similar events in the future.

Keywords: WRF model; Precipitation simulation; Topographic impacts; Urbanization; Beijing area

https://doi.org/10.5194/egusphere-2025-4746
Preprint. Discussion started: 21 October 2025

1. Introduction

In the precipitation process, water vapor in the atmosphere condenses and falls to the Earth's surface in the form of liquid or solid as a crucial component of the global water cycle (Gimeno et al., 2010; Trenberth et al., 2003). Unlike other climatic variables, precipitation is typically discontinuous in a given location and its temporal distribution is uneven (Pendergrass and Knutti, 2018; Wu et al., 2021). Extreme precipitation events, characterized by high precipitation rates over short durations or prolonged accumulated precipitation, often result in natural disasters such as floods and landslides. These events can disrupt ecosystems, agricultural production, and cause significant economic damage and loss of life (Ayat et al., 2022; Mahoney, 2016; Yu et al., 2024). Therefore, extreme precipitation has become a major focus of research in weather and climate research (Dai et al., 2024; Li et al., 2024a; Sun et al., 2021; Zhang et al., 2022).

Numerical simulations of extreme precipitation events play crucial roles in enhancing our understanding of the mechanisms and hydrological processes involved, providing essential tools for their prediction and assessment (Mahoney, 2016). Based on numerical simulations of precipitation, it is possible to evaluate the relative impacts of various factors on precipitation events and the underlying mechanisms to facilitate the development of mitigation strategies to reduce the possibility of similar events in the future. Land surface processes can have various effects on extreme precipitation. In particular, a nonuniform land surface can affect the near-surface pressure gradient due to the inhomogeneous distribution of sensible and latent heat fluxes, thereby stimulating local mesoscale circulation (Wang and Zhong 2014). The roughness anomalies induced by cities can prolong the stagnation time of a rainstorm system and increase local precipitation near cities (Pielke 2001).

Topography is one of the most critical factors in land-air interaction, due to its capacity to alter precipitation patterns through a variety of complex processes (Smith, 2006). The mountain ranges can modify the spatial distribution of precipitation by blocking and uplifting air masses to alter the atmospheric properties at different

https://doi.org/10.5194/egusphere-2025-4746
Preprint. Discussion started: 21 October 2025

elevations on both the windward and leeward sides (Cornejo et al., 2024; Davolio et al., 2009; Lin et al., 2001; Wei et al., 2023).The orographic forcing can also influence the temperature and humidity of the lower atmosphere, which alters the distribution of convection by controlling the buoyancy of air masses (Nicolas and Boos, 2024) to increase the moisture content over the foothills, thereby promoting precipitation in these regions (Du et al., 2020; Gao et al., 2021; Xia and Zhang, 2019; Yin et al., 2020). In addition, the thermodynamic differences between mountainous areas and plains give rise to local thermal circulations, which are among the physical processes that influence the spatial distribution and diurnal variation of precipitation (Chen et al., 2014; He and Zhang, 2010). The setting of altitude in the numeric model can affect the regional water vapor flux, especially the channel of moisture in the lower and middle troposphere (Saurral et al., 2015). Therefore, the influence of topography is particularly significant for determining precipitation patterns in mountainous regions and surrounding plains.

Due to increases in the intensity of human activities, altered land use patterns caused by urbanization are key factors that need to be considered in precipitation events (Dou et al., 2015; Huang et al., 2019; Niyogi et al., 2011). The emergence of urban areas has led to the development of unique urban canopies and urban boundary layers, giving rise to the urban heat island (UHI) effect, which significantly increases the surface roughness, thereby causing convergence and upward lifting in the lower atmosphere (Bornstein and Lin, 2000; Hjelmfelt, 1982). The UHI effect can enhance boundary layer turbulence mixing by increasing the surface heat flux to strengthen boundary layer instability and lead to precipitation (Holst et al., 2016; Nie et al., 2017). This effect is especially significant for modifying mesoscale and small-scale circulations and convection (Dixon and Mote, 2003; Oke, 1982; Yin et al., 2020; Zhang et al., 2017), which induces convective activity in urban and surrounding areas, and changes in precipitation patterns (Fu et al., 2024a; Li et al., 2011; Yang et al., 2017). The presence of the urban canopy can also slow down the flow of convective systems to prolong the duration of precipitation events (Wang and Zhong, 2014; Yan

https://doi.org/10.5194/egusphere-2025-4746
Preprint. Discussion started: 21 October 2025

et al., 2023; Yu and Liu, 2015). However, how the precipitation response to urbanization varies under different degree of land use change climatic backgrounds (Wang et al., 2015). The "urban rain island" effect may be observed in some coastal cities with abundant moisture transport (Jauregui and Romales, 1996; Wang et al., 2018), whereas the depletion of moisture in the lower atmosphere caused by urban activities may lead to the "urban dry island" effect in relatively arid cities (Freitag et al., 2018; Wang and Gong, 2010). Therefore, the mechanisms that urbanization influences extreme precipitation events are complex, necessitating further research to clarify the roles of cities in these events.

Beijing is located in the northwest of the North China Plain in the transitional zone among the Taihang Mountains, Yanshan Mountains, and North China Plain. The western part of Beijing is located in the Taihang Mountains region, the northern part is in the Yan Mountains region, and the central and southwestern regions are located on the North China Plain. It is an international metropolis with a population of over 10 million and its surrounding areas have experienced rapid urbanization since the 1980s. In recent years, Beijing and neighboring areas of Hebei and Tianjin have frequently experienced high-intensity extreme precipitation events during the summer months (Tewari et al., 2022; Yu et al., 2017; Zhang et al., 2013; Zhong et al., 2015). Some previous studies have provided evidence of increases in the frequency of extreme precipitation events in large cities (Liang and Ding, 2017), and Beijing is a representative region for studying these events.

In this study, we analyzed an extreme precipitation event that occurred in Beijing from July 29 to August 2, 2023, and investigated simulation results for this event using the Weather Research and Forecasting model (WRF). The accumulated precipitation distribution had a clear pattern, with higher amounts in the southwestern mountainous areas and lower amounts in the northeastern regions for this precipitation event. Therefore, both the orographic effect and urban land use could have potentially influenced the precipitation spatial pattern. Several experiments were selected to assess the impacts of changes in the underlying surfaces The causes of the

https://doi.org/10.5194/egusphere-2025-4746
Preprint. Discussion started: 21 October 2025

event and the related mechanisms were examined, as well as quantifying the effects of topography, land use, and other factors on the precipitation event.

2. Data and Methodology

2.1. Study Area and Event Description

The present study focused on the "7 31" event that occurred in Beijing area (shown in region D04 in Figure 1) during July 2023. From July 29 to August 2, 2023, a severe and prolonged heavy rainfall event affected Beijing and neighboring areas of Tianjin and Hebei. This event was driven by the residual forces of Typhoon Doksuri moving northward and the influence of Typhoon Khanun. During this event, average precipitation in the Beijing region exceeded 300 mm, where the most affected areas, including Fangshan and Mentougou districts, recorded average accumulated rainfall amounts greater than 500 mm. The maximum rainfall in the city occurred at Wangjiayuan Reservoir in Changping, with 744.8 mm (Li et al., 2024b). The rainstorm also triggered severe flooding and urban waterlogging, resulting in significant damage to infrastructure and property across the entire region.

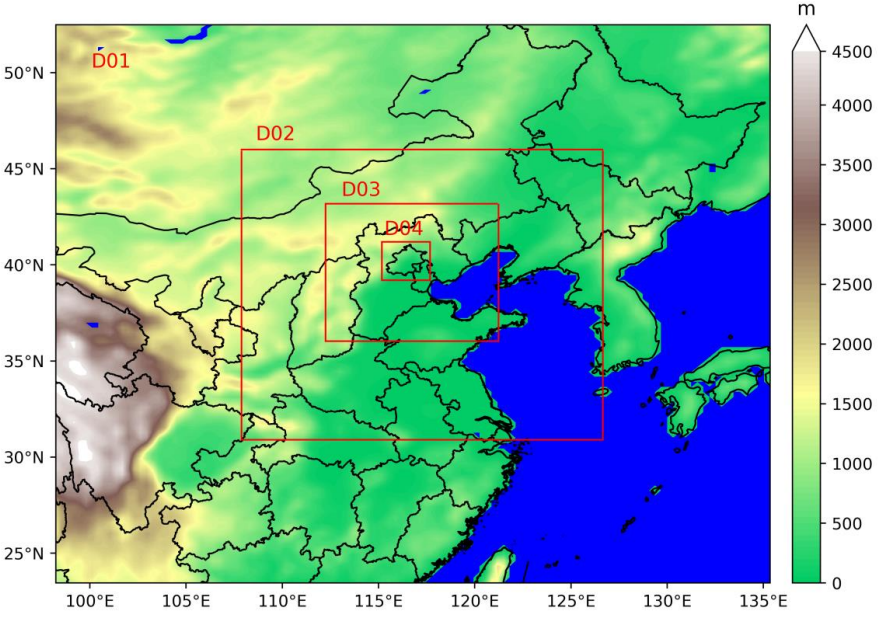

Figure 1: Study area and domains of the numerical model. The coordinates of the different

https://doi.org/10.5194/egusphere-2025-4746
Preprint. Discussion started: 21 October 2025

domains are as follows: D01: 98.23 °E to 135.35 °E, 23.45 °N to 52.49 °N; D02: 107.88 °E to 126.65 °E, 30.91 °N to 46.00 °N; D03: 112.25 °E to 121.23 °E, 36.04 °N to 43.19 °N; D04: 115.17 °E to 117.68 °E, 39.21 °N to 41.20 °N. The grid spacings for each domain are 27 km, 9 km, 3 km, and 1 km, respectively.

2.2. Data Descriptions

In the experiment, ERA5 global reanalysis data were used to provide initial and boundary conditions for the WRF model (Hersbach et al., 2020). The data selected for this study has a temporal resolution of 1 h and a spatial resolution of 0.25 ° × 0.25 °. To investigate the impact of land use in the simulation, updated land use data were used to replace the default land use data within the WRF model. The data used in this study were acquired from the Moderate-resolution Imaging Spectroradiometer (MODIS) MCD12Q1 V6 product for the year of 2020, with a spatial resolution of 500 m (Friedl, 2019).

The analysis involves the movement and spatial variability of extreme precipitation systems, which cannot be adequately captured by meteorological observation stations. Alternatively, satellite-derived precipitation products are commonly used and have reliabilities in estimating spatial precipitation distribution (Bhattarai and Talchabhadel, 2024). Among them, the Climate Prediction Center Morphing technique (CMORPH) product can offer high temporal and spatial resolution and has demonstrated advantages in capturing extreme precipitation patterns (Liu et al., 2022), which has been validated over China in previous studies (Ebert et al., 2007; Jiang et al., 2016; Sun et al., 2016). CMORPH data based on a combination of microwave and infrared precipitation data provide high temporal and spatial resolution global precipitation data (Joyce et al., 2004). Therefore, using CMORPH data to validate the simulation results was highly reasonable. In this study, CMORPH data with a temporal resolution of 30 min and spatial resolution of 8 km × 8 km were used for precipitation validation.

2.3. Model Description and Experimental Design

WRF model version 4.5.1 was selected as the numerical simulation tool for this

https://doi.org/10.5194/egusphere-2025-4746
Preprint. Discussion started: 21 October 2025

study (Skamarock et al., 2019). The simulation period covered from 00:00 UTC July 28th, 2023, to 00:00 UTC on August 2nd, 2023, where the first 24 h were used for model spin-up. A four-level nested domain was utilized with grid spacings (grid numbers) of 27 km (120 × 122), 9 km (181 × 187), 3 km (259 × 268), and 1 km (217 × 226). Domain D01 covered most of central and eastern China and domain D04 focused on the Beijing region (Figure 1). In addition, 49 vertical layers were employed in the simulation and the upper boundary was set at 50 hPa. The physical packages used are summarized in Table 1. To ensure that the large-scale circulation in the experiment closely matched the ERA5 input data to ensure more accurate results, spectral nudging was applied to the D01 domain in terms of the zonal and meridional wind, temperature, and specific humidity (Miguez-Macho et al., 2004; Spero et al., 2014). The assimilation coefficient was set to 3×10^{-4} s^{-1}, and the cut-off wave number was set to 3 in both the zonal and meridional directions. The hourly output for region D04 was used in the following analysis.

Table 1: Model configurations selected for WRF in this study

Options	Settings
Surface layer scheme	Revised MM5 Monin-Obukhov scheme (Jiménez et al. 2012)
PBL scheme	Yonsei University scheme(Hong et al. 2006)
Land Surface scheme	unified Noah land-surface model (Chen and Dudhia 2001)
Shortwave radiation	Dudhia scheme (Dudhia 1989)
Longwave radiation	RRTM scheme (Mlawer et al. 1997)
Microphysics scheme	WSM6 (Hong 2006)
Cumulus scheme	Kain-Fritsch scheme for D01 & D02 (Kain 2004)

https://doi.org/10.5194/egusphere-2025-4746
Preprint. Discussion started: 21 October 2025

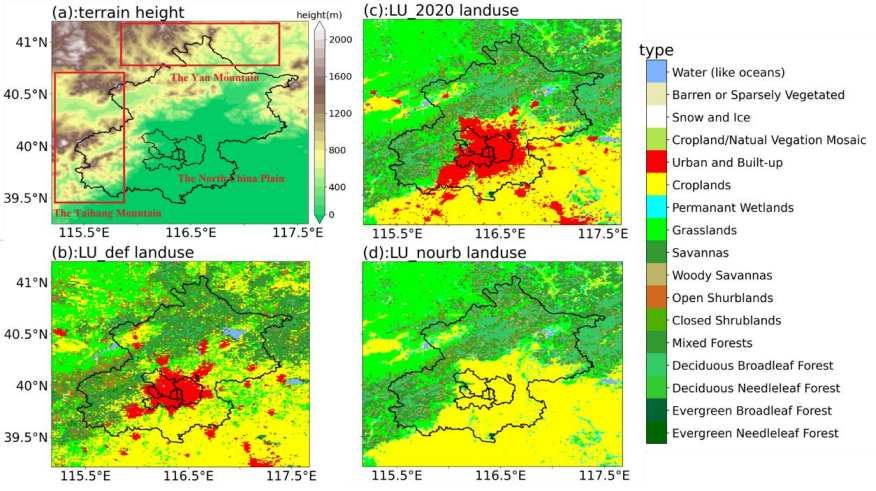

Figure 2: Terrain elevation and land use types in domain D04 in the experiment. (a) Terrain elevation in region D04. (b) Default land use types in region D04. (c) Land use types in region D04 after replacement. (d) Land use types in region D04 with urban areas replaced by cropland.

To improve the accuracy when simulating the impacts of urban areas on the precipitation event, the single-layer urban canopy model (SLUCM) (Chen et al., 2011) was used to enhance the accurate simulation of the evolution of dynamic and thermodynamic processes in urban environments (Yu and Liu, 2015; He et al., 2023). Different sensitivity test groups were set-up to explore the effects of land use and topography on the precipitation event, and the differences between these test groups were analyzed. The default land use types in WRF (represented as LU_def in Figure 2(b)) were replaced with land use data from the MODIS MCD12Q1 V6 product for the year 2020 (represented as LU_2020 in Figure 2(c)).

To explore the impact of orography, based on the LU_2020 scheme, areas in domain D03 and D04 with elevations greater than 100 m were set to 100 m (represented as LU_nohgt) in order to explore the impacts of the Taihang and Yan Mountains on precipitation. In addition, urban areas in the land use data were replaced with agricultural land (represented as LU_nourb in Figure 2(d)) to examine the results in the absence of urban surface effects.

https://doi.org/10.5194/egusphere-2025-4746
Preprint. Discussion started: 21 October 2025

2.4. Verification Statistics

To investigate the impacts of land use changes on the simulation results, the accumulated precipitation, precipitation intensity from LU_2020 simulations with observed data were analyzed. To further validate the accuracy of the simulated precipitation, the average precipitation intensity obtained from the simulations was compared with the precipitation intensity from CMORPH data. The following evaluation metrics were used for validation: mean absolute error (MAE), root mean square error (RMSE), and correlation coefficient (R). The specific formulas for these metrics are as follows:

$$MAE = \frac{1}{n}\sum_{i=1}^{n}|S_i - O_i| \quad (1)$$

$$RMSE = \sqrt{\frac{\sum_{i=1}^{n}(S_i - O_i)^2}{n}} \quad (2)$$

$$R = \frac{\sum_{i=1}^{n}(S_i - \bar{S})(O_i - \bar{O})}{\sum_{i=1}^{n}(S_i - \bar{S})^2 \sum_{i=1}^{n}(O_i - \bar{O})^2} \quad (3)$$

where S_i and O_i are the simulated and observed values, respectively.

3. Results

3.1. Evolution of the Precipitation Event

The meteorological background in Figure 3(a), 3(d), 3(g), 3(j) shows the initial stage of the EP event. At 00:00 UTC July 30th, the residual circulation of Typhoon Doksuri moved northward and weakened as it advanced inland. A high-pressure dam over Mongolia and the subtropical high over the Pacific formed a barrier that blocked the movement of upper-level air masses. The precipitable water over Beijing increased from 49.43 mm to 56.63 mm, the relative humidity rose from 86.06% to 91.88%, and the equivalent potential temperature increased by around 5 K. By 00:00 UTC on July 31st (Figures 3(b), 3(e), 3(h), 3(k)), the residual circulation of Typhoon Doksuri was almost nonexistent and its remnants were transported northward together

https://doi.org/10.5194/egusphere-2025-4746
Preprint. Discussion started: 21 October 2025

with moisture from the newly formed Typhoon Khanun in the western part of Pacific. In addition, the high-pressure ridge over the northern region gradually strengthened and moved southward. These conditions led to an increase in moisture over Beijing, which resulted in the precipitable water remaining above 70 mm, the relative humidity exceeding 95%, and the equivalent potential temperature rising above 350 K in the western mountainous areas. This process continued until around 12:00 UTC August 1st (Figures 3(c), 3(f), 3(i), 3(l)). At this time, the original high-pressure block over Beijing gradually shifted southward and the upper-level air flow moved northeastward along the isobars. The precipitable water, relative humidity, and equivalent potential temperature all then declined significantly, and the extreme precipitation event began to gradually subside.

In our experiments, the spectral nudging was applied within the D01 domain for each scheme to capture large-scale circulation features, showed in Figures S1-S3 for LU_2020, LU_nohgt, and LU_nourb, respectively. The results indicate that the simulated large-scale circulation on stages of the precipitation event is generally consistent with that of the ERA5. A distinct remnant low-pressure center associated with Typhoon Doksuri can still be found in Figures S2b and S2e. This is likely due to the weakened orographic blocking effect after removing the terrain in LU_nohgt, which allows the low-pressure system to continue moving northward and exerts precipitation over the Beijing-Tianjin-Hebei region. In contrast, a comparison of Figures S1 and S3 shows that changes in urban land use have a negligible impact on large-scale circulation. Therefore, the LU_nohgt and LU_nourb simulations exhibit similar large-scale flow patterns to LU_2020, suggesting that the observed differences in precipitation induced by changes in local circulation. Given the limited influence of topographic and land use changes on large-scale atmospheric circulation, this study subsequently concentrates on analyzing variations at the local scale.

https://doi.org/10.5194/egusphere-2025-4746
Preprint. Discussion started: 21 October 2025

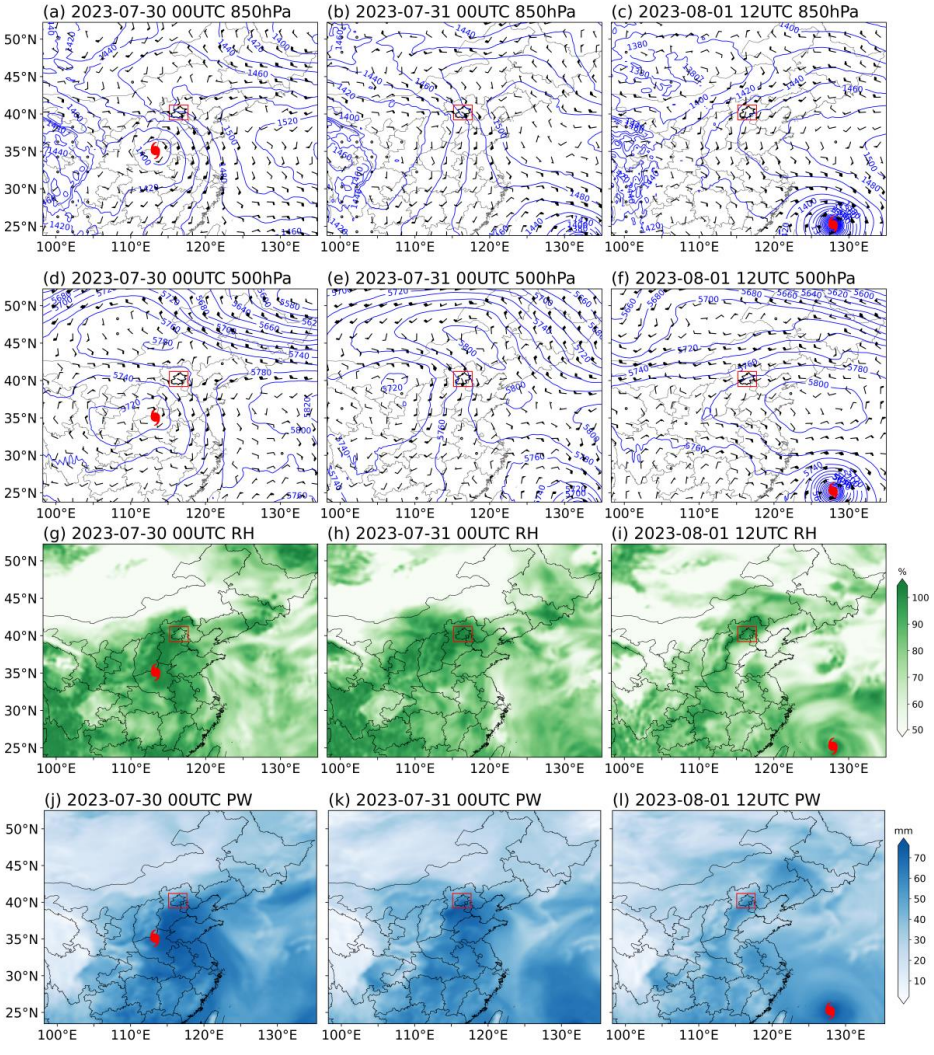

Figure 3: Upper-level weather pattern diagrams for the precipitation event (source: ERA5): (a)–(c) 850 hPa upper-level weather patterns; (d)–(f) 500 hPa upper-level weather patterns; (g)-(i) 850 hPa relative humidity; and (j)-(l) precipitable water at 00:00 UTC July 30th, 00:00 UTC July 31st and 12:00 UTC August 1st. The blue solid lines represent geopotential height contours, the green shading indicates the relative humidity, and the blue shading represents the precipitable water. The typhoon symbol in 3(a), 3(d), 3(g), 3(j) representing residual circulation center of typhoon Doksuri, and typhoon symbol in 3(c), 3(f), 3(i), 3(l) representing location of typhoon Khanun.

3.2. Analysis of Variations in Precipitation

3.2.1. Impacts of Updated Land Use Data

https://doi.org/10.5194/egusphere-2025-4746
Preprint. Discussion started: 21 October 2025

Figure 4 compares the WRF simulation results with the satellite-based quantitative precipitation estimates. As shown in Figure 4(a–b), the spatial distributions of accumulated precipitation were similar, with higher precipitation in the southwestern mountainous areas and lower precipitation in the northeastern region. This illustrated that the pattern of LU_2020 scheme closely matched the accumulated precipitation distribution obtained by CMORPH. In addition, LU_2020 scheme obtained maximum precipitation values exceeding 800 mm in the southwestern mountainous region, which was slightly higher than the observed value (with a maximum of less than 700 mm), while in the northeastern part of Beijing, the simulated precipitation was slightly lower than observed. The simulated average precipitation intensity results also matched closely with the observed spatial distribution (Figure 4(c-d)) although LU_2020 slightly underestimated the precipitation intensity compared with CMORPH (Figure 4(e)). Thus, the WRF simulation results provided a reasonable representation of the overall precipitation event, and the LU_2020 simulation results were used to analyze the differences due to topography and land use.

https://doi.org/10.5194/egusphere-2025-4746
Preprint. Discussion started: 21 October 2025

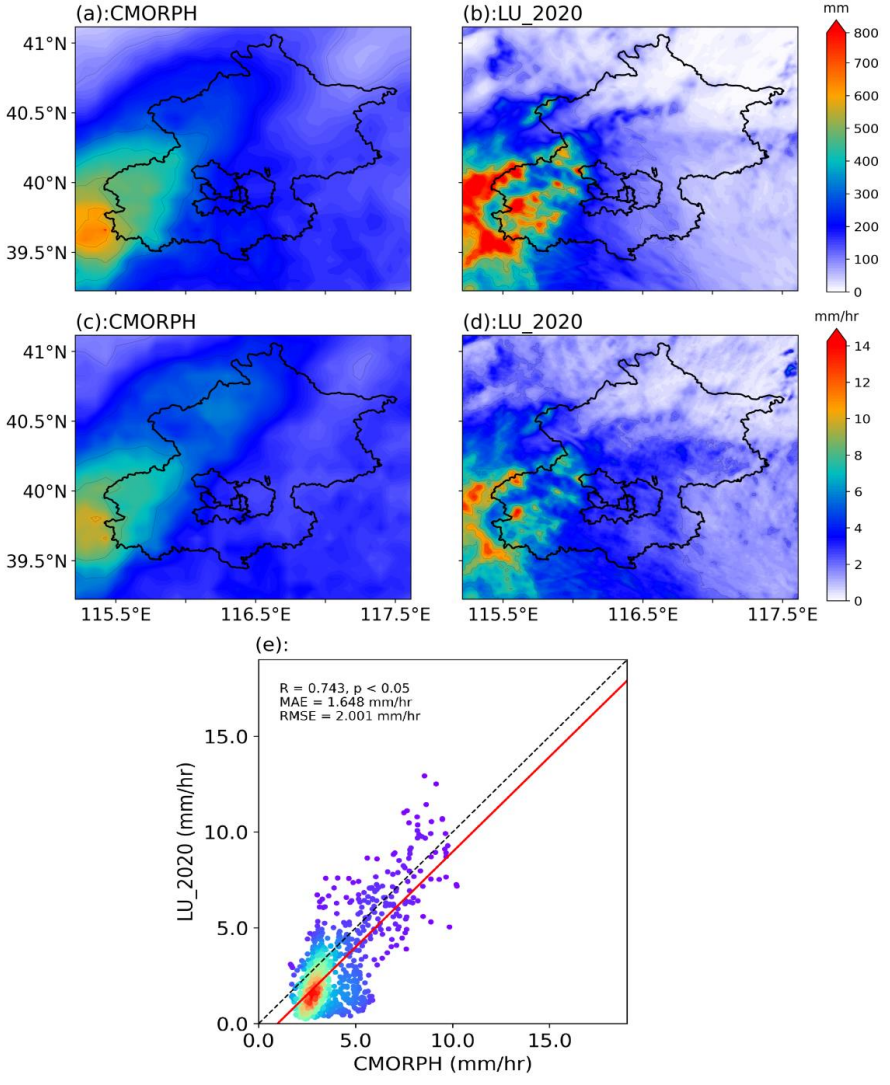

Figure 4: Comparison of simulated and observed precipitation: (a)–(b) accumulated precipitation for CMORPH and LU_2020, respectively; (c)–(d) average precipitation intensity for CMORPH and LU_2020; and (e) scatter plots for the precipitation intensity for CMORPH and LU_2020, while the red line represents the linear regression.

3.2.2. Impacts of Topography

Figure 5 (a) and 5(c) show the spatial distributions of the average precipitation intensity and accumulated precipitation before and after removing the topography. It illustrated that the removal of terrain elevation significantly indeed altered the spatial

https://doi.org/10.5194/egusphere-2025-4746
Preprint. Discussion started: 21 October 2025

pattern of accumulated precipitation throughout the simulation period. Compared to the LU_2020 scheme, the LU_nohgt exhibited a marked decrease in cumulative precipitation over the southwestern portion of D04 area. Conversely, a slightly increase in precipitation was generated in southern Beijing in LU_noght. The accumulated precipitation was 229.42 mm higher, accounting for over 41.34% of the total precipitation. In contrast, in the central urban and northern regions of Beijing, the total precipitation was 83.59 mm lower, representing 43.50% of the total precipitation. This is primarily attributed to removal of the Taihang mountainous region. As the blocking effect caused by mountain on the remnant circulation was greatly diminished. This allowed low-pressure system persist a long period within Beijing region and facilitated its northward progression. The lack of orographic lifting ultimately leads to different precipitation distributions over the Beijing region.

Figure 6(a) and 6(b) show the changes in precipitation for each time period at the central latitudes between 39.5°N and 40.1°N. From 00:00 to 10:00 on July 30, precipitation primarily occurred in the transition zone between the city and mountains, where the terrain features caused heavy precipitation in the mountainous areas in the morning on July 30. From July 31 to 12:00 on August 1, precipitation mainly occurred in the mountainous areas, and the impact of topography became more significant. In the LU_nohgt scheme, precipitation in the mountainous areas stopped around 12:00 on July 31, whereas in the LU_2020 scheme, precipitation continued until around 00:00 on August 1, i.e., 12 h longer. Thus, the topography had a significant impact on the second phase of precipitation. In terms of the precipitation intensity and distribution, the presence of the topography altered the timing of heavy precipitation in the mountainous areas and intensified the precipitation in the central urban area around 12:00 on July 31.

3.2.3. Impacts of Land Use

Figure 5(b) and 5(d) show the impact of the urban land surface compared with removal of the urban land surface. The spatial distributions of the average

https://doi.org/10.5194/egusphere-2025-4746
Preprint. Discussion started: 21 October 2025

precipitation intensity and accumulated precipitation were quite similar for LU_2020 and LU_nourb, with no significant difference in the overall precipitation pattern. The presence of urban areas did not significantly affect the central urban region of Beijing. However, in the southwestern mountainous region of Beijing, the average accumulated precipitation was 88.07 mm lower (the total precipitation was 15.87% lower).

Figure 6(a) and 6(c) show the variations in precipitation with longitude and time for the central urban region corresponding to the central latitude. From 00:00 to 10:00 on July 30, the range and intensity of precipitation differed little between the city and the transition zone to the mountains, indicating that changes in land use had minor effects during this period. From July 31 to 12:00 on August 1, the overall total precipitation was lower in the LU_2020 scheme, although more precipitation occasionally occurred in the western part of the city in the LU_2020 scheme compared with the LU_nourb scheme. There was no significant difference in the duration of precipitation between the two experimental groups.

Therefore, during the precipitation event, both topography and land use altered the precipitation pattern, where the most significant changes in precipitation occurred in the southwestern part of Beijing. To understand the main causes of the differences in precipitation, we selected the region denoted by the purple box in Figure 5 for more detailed analysis of the mechanism as it was affected most by the land surface (referred to as RegP in the following). In addition, due to the prolonged nature of the event, we selected three time periods with notable differences in the precipitation distribution according to Figure 5 for further mechanistic analysis to explore the effects of topography and land use on the event. The three periods of interest were: 01:00–04:00 UTC on July 30th (referred to as T1), 03:00–06:00 UTC on July 31st (referred to as T2), and 12:00–15:00 UTC on July 31st (referred to as T3).

https://doi.org/10.5194/egusphere-2025-4746
Preprint. Discussion started: 21 October 2025

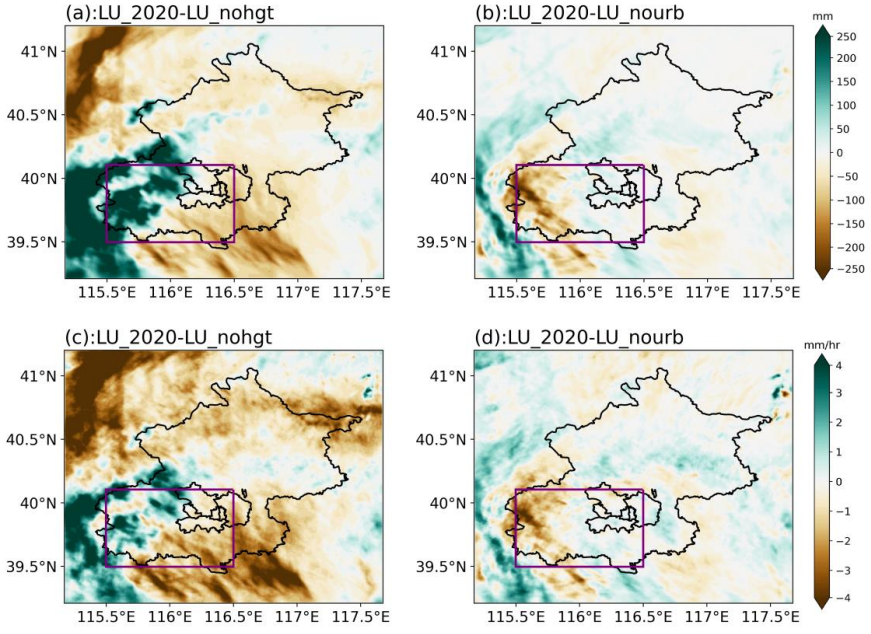

Figure 5: Effects of terrain and urban underlying surface changes on accumulated precipitation and average precipitation intensity from 00:00 July 29th to 00:00 UTC August 2nd: (a) and (c) differences in accumulated precipitation and average precipitation intensity between the simulation using 2020 land use data and the scheme where terrain higher than 100 m was removed; and (b) and (d) differences in accumulated precipitation and average precipitation intensity between the simulation using 2020 land use data and the scheme where urban land use was removed. The purple area (RegP) indicates the region in Beijing where the difference in precipitation was significant.

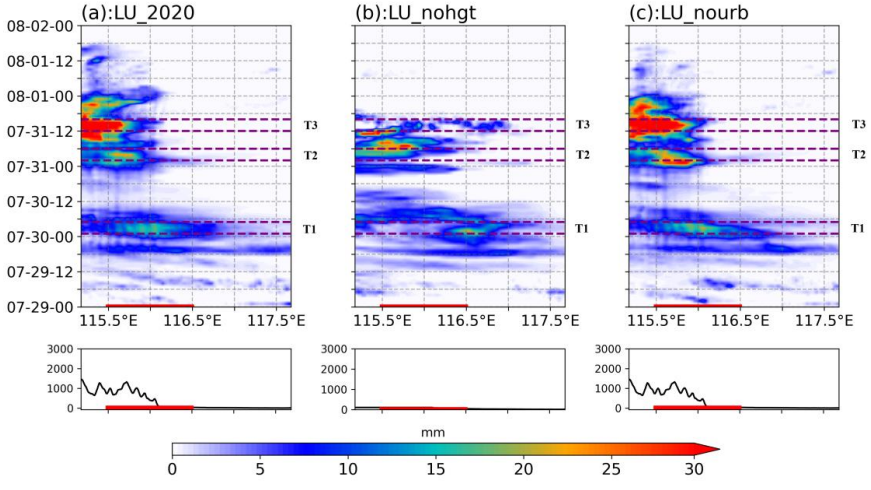

Figure 6: Hovmöller diagrams from 00:00 July 29th to 00:00 UTC August 2nd for the three

https://doi.org/10.5194/egusphere-2025-4746
Preprint. Discussion started: 21 October 2025

experimental groups: (a) LU_2020 scheme, (b) LU_nohgt scheme, and (c) LU_nourb scheme, within the range of 39.8 °N–40.1 °N. Terrain heights at corresponding latitudes are shown.

3.3. Physical Mechanism

3.3.1. Energy and Water Vapor Budget Comparison

First, energy and water vapor fluxes were compared among different experimental groups. As shown in Figure 7, all experimental groups exhibited distinct diurnal variations, with significant increases in both the sensible heat flux and latent heat flux after 00:00 UTC August 1st. This phenomenon was mainly due to the end of the extreme precipitation event, where the increased surface energy input strengthened both the sensible and latent heat fluxes.

In RegP, both the sensible and latent heat fluxes were slightly higher than the regional averages. The topographic effects on the latent heat flux were more pronounced, especially during periods T1 and T2 (Table 2), as the removal of topographic features leads to an increase in both surface pressure and temperature for the high elevated regions. It enhances near-surface humidity and alters the latent heat flux across the region. The relatively lower latent heat flux observed in LU_nohgt during period T3 could be attributed to the extended duration of the precipitation event caused by the removal of topographic effects.

Compared with period T1, urban surfaces led to average reductions in the latent heat flux of 16.70 W/m^2 and 7.06 W/m^2 in region RegP during periods T2 and T3, respectively, mainly due to the lower permeability of urban surfaces compared with croplands reducing the regional humidity, and thus decreasing the latent heat flux across the area. During period T1, the impact of urbanization on the moisture content in region RegP was less pronounced, suggesting that removing urban areas had minimal effect on the water vapor content in this stage. Changes in the sensible heat flux (Figure 7(a)) due to urbanization were also concentrated in RegP. The topography in the urban area varied little in the three experimental groups. When the land use shifted from urban surfaces to croplands, the reduced urban heat emissions significantly decreased the sensible heat flux in the central urban area, so it was lower

https://doi.org/10.5194/egusphere-2025-4746
Preprint. Discussion started: 21 October 2025

than those in the other groups. It was notable that changes in the latent heat flux (Figure 7(b)) in region RegP were more complex than those in the sensible heat flux, which could be attributed to different changes in the water vapor content.

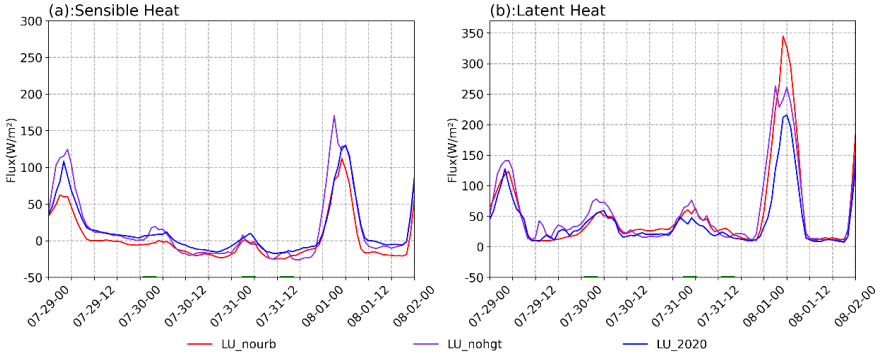

Figure 7: Temporal variations in energy balance during the event for the LU_2020, LU_nohgt, and LU_nourb schemes. In (a) and (b), solid lines represent the sensible and latent heat fluxes within the precipitation anomaly area RegP for each scheme.

Table 2: Average flux values in RegP region during precipitation process (unit: W/m^2)

flux	Scheme	T1	T2	T3	All-time
Sensible Heat	LU_2020	7.28	5.98	-15.36	14.04
	LU_nohgt	10.85	-0.62	-18.47	16.25
	LU_nourb	-4.19	-0.92	-22.91	1.83
Latent Heat	LU_2020	46.38	41.82	19.04	41.85
	LU_nohgt	63.38	67.18	17.68	58.00
	LU_nourb	42.74	58.52	26.10	56.29

Figure 8 shows the magnitudes of the water vapor flux at the four boundaries of region RegP for LU_2020. Specifically, the moisture inflow across the southern boundary (Figure 8a, e, i) and the eastern boundary (Figure 8d, h, l) represent meridional and zonal sources of water vapor entering the region. The outflow across the northern boundary (Figure 8a, e, i) and the eastern boundary reflect the moisture exported from the region. The difference between the inflow and outflow moisture flux indicates net moisture income in each time period. During period T1, water vapor was transported southward at low latitudinal levels along the southern boundary, with northward transport of water vapor at high levels. As Taihang Mountains extend in a

https://doi.org/10.5194/egusphere-2025-4746
Preprint. Discussion started: 21 October 2025

southwest-northeast direction in the study area, the eastern zonal airflow blocked by the Mountainous area and shifted southward. At the northern boundary, there was almost no net meridional moisture transport, mainly due to topographic effects that confined moisture transport towards north.

During periods T2 and T3, the water vapor flux distributions were similar. Due to the evolution of circulation patterns between T2 and T3, the eastward water vapor flux was greater in T2, while meridional moisture flux was weaker. In addition, the eastward moisture transport during T3 became more concentrated in low layers. Compared with T1, the northward water vapor flux at the southern boundary was significantly increased. As in T2 and T3, the southward transport increased and lead to strong meridional motions in the Taihang mountainous area, and strong uplift motion in mountainous area. Consequently, the mountainous areas may have been more prone to intense convective weather events due to the sufficient water vapor and air uplift conditions during T2 and T3.

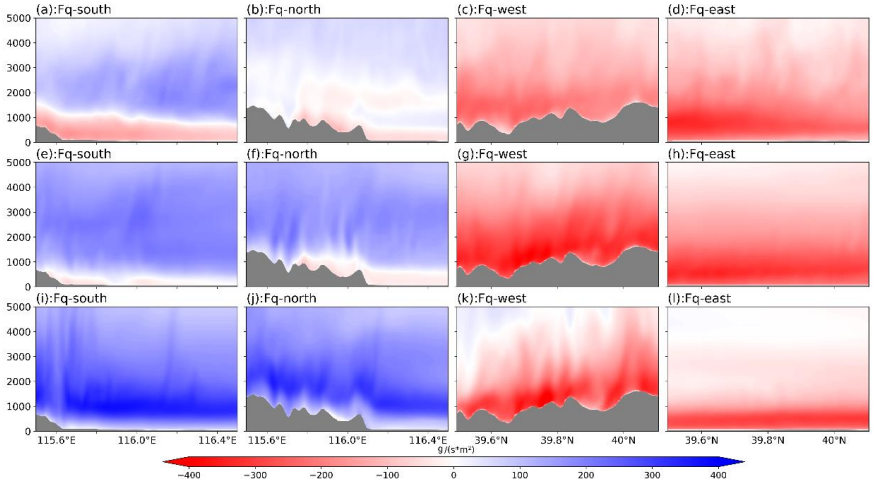

Figure 8: Distribution of water vapor flux magnitude in the LU_2020 scheme across latitude-height/longitude-height coordinates of RegP. Figures show the water vapor flux magnitude for time periods T1 (a–d), T2 (e–h), and T3 (i–l), with fluxes from the south (a, e, i), north (b, f, j), west (c, g, k), and east (d, h, l). Positive and negative water vapor flux values correspond to positive and negative directions of meridional and zonal wind speed, respectively.

Orographic height significantly impacted water vapor flux transport, as shown by

https://doi.org/10.5194/egusphere-2025-4746
Preprint. Discussion started: 21 October 2025

the differences in the water vapor distribution between LU_2020 (Figure 8(a–l)) and LU_nohgt (Figure 9(a1–l1)). From a latitudinal perspective, topography considerably influenced the water vapor within RegP. Due to orographic effects, water vapor was lifted and prevented, and thus the northward water vapor flux to the southern boundary was reduced in the LU_2020 scheme compared with the LU_nohgt scheme (Figures 9(a1), 9(e1), and 9(i1)). However, the northward water vapor flux at the northern boundary remained relatively large in the LU_nohgt scheme, so the water vapor input amount from the latitudinal direction increased. From a meridional perspective, the meridional water vapor flux input increased substantially during the T3 period, resulting in a noticeable rise in the water vapor in the whole region at that time. Furthermore, in addition to being influenced by large-scale circulation, the easterly winds were prevented and diverted by the orographic effect of the mountains to the west of Beijing, leading to a modest increase in the magnitude of the southward water vapor flux at the southern boundary in the lower atmospheric layers.

The impacts of the urban surface on water vapor transport are shown in Figure 9(a2–l2). Comparison of the water vapor distributions between LU_2020 and LU_nourb found no significant difference in the water vapor flux during periods T1 and T2, but during period T3, the differences mainly appeared at the northern and western boundaries of region RegP. At the northern boundary of region RegP, the presence of the urban surface led to a higher water vapor flux compared with the LU_nourb scheme (Figure 9(j2)). At the western boundary, the westward water vapor flux was noticeably higher compared with LU_nourb (Figure 9(k2)). These differences of moisture flux between different schemes mainly due to wind speed in lower troposphere. As urban land use can influence local atmospheric circulation, this strong ascent induces horizontal convergence and a subsequent conversion of horizontal momentum into vertical motion. Such momentum redistribution can reduce the horizontal wind speed, particularly within the convectively active region, leading to a reduction in moisture flux across west and north boundaries.

https://doi.org/10.5194/egusphere-2025-4746
Preprint. Discussion started: 21 October 2025

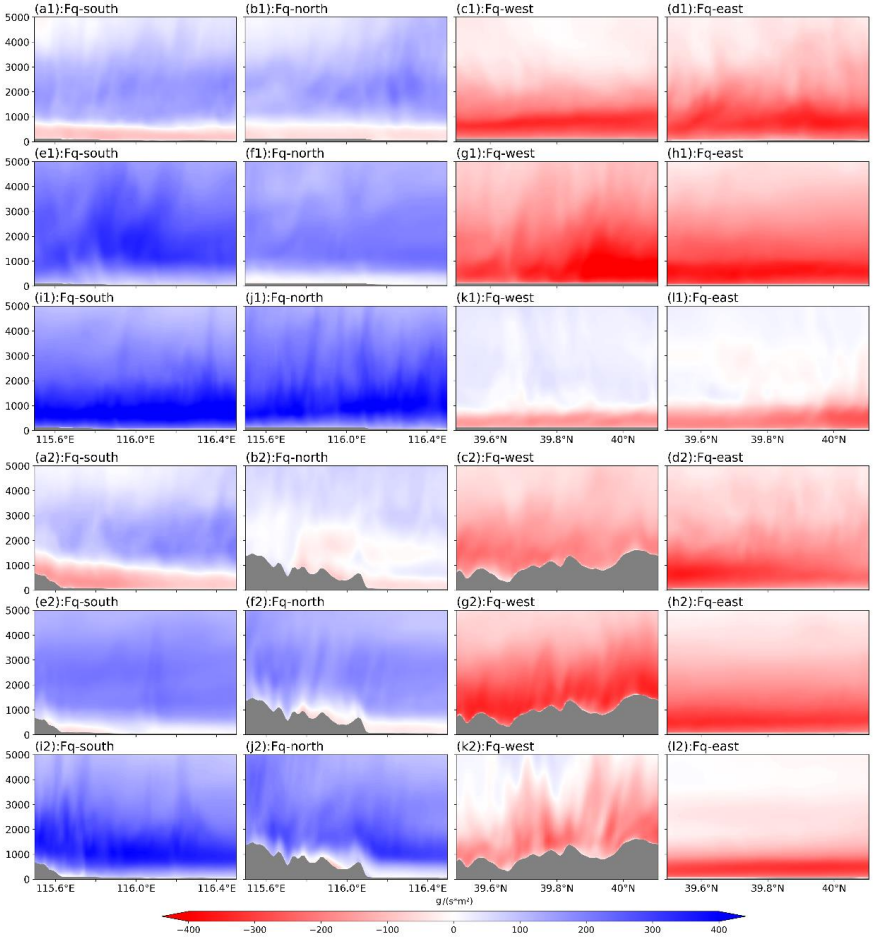

Figure 9: Water vapor fluxes as shown in Figure 8, where a1–l1 depict the magnitude of the water vapor flux from four directions in the LU_nohgt scheme, and a2–l2 depict the magnitude of the water vapor flux from four directions in the LU_nourb scheme.

3.3.2. Differences in Near-surface Physical Variables

Near-surface physical quantities did not directly determine the magnitude of precipitation, but changes in the underlying surface were directly reflected in variations in the near-surface physical quantities, which then influenced the upper atmosphere and subsequently affected the intensity of precipitation. Figure 10(a–c) illustrates the horizontal distributions of the equivalent potential temperature, wind speed, and humidity during the three precipitation time periods.

https://doi.org/10.5194/egusphere-2025-4746
Preprint. Discussion started: 21 October 2025

During period T1 (Figure 10(a)), precipitation was mainly concentrated in the southwestern mountainous and central region. The equivalent potential temperature over Beijing remained between 346–347 K, but it was slightly lower than the regional average in RegP. These results are consistent with the flux changes shown in Figure 7. The lowest equivalent potential temperature in Beijing was observed in the northwestern mountainous areas (343 K). In addition, the 2-m relative humidity in Beijing during period T1 remained at an average value over 90%, and the 10-m wind direction was influenced by circulation and topographic blocking, resulting in a northeastern wind. The wind direction was more erratic in mountainous areas, where the relative humidity was slightly lower than that in the Beijing plains, and the precipitation was also relatively lower compared with the southern regions.

During period T2 (Figure 10(b)), the precipitation entered the initial stage of the second precipitation phase, where the precipitation mainly occurred in the southwestern mountainous areas. The southerly warm and moist air currents transported water vapor and also provided the energy required for precipitation. The equivalent potential temperature was higher in southern Beijing, and it decreased from south to north, which was linked to the energy loss as the air moved northward. This variation was associated with the energy dissipation process as the airflow moved northward. The overall equivalent potential temperature gradually increased over time (rising from 351.6 K at 03:00 on July 31 to 354.3 K at 06:00 on July 31).

In period T3 (Figure 10(c)), the precipitation remained intense and the areas with the most intense precipitation were still located in the western mountainous areas of Beijing. The overall distribution of the equivalent potential temperature during this period was similar to that in period T2, and the highest values were still located in the southwestern mountainous areas of Beijing. The average equivalent potential temperature in Beijing remained within a range of 355–356 K. The overall relative humidity in the region was higher compared with period T2 (rising to 90.0%). The wind direction in the central urban area shifted slightly to the north due to the influence of the northerly air currents, but there was no significant change in the wind

https://doi.org/10.5194/egusphere-2025-4746
Preprint. Discussion started: 21 October 2025

speed compared with period T2.

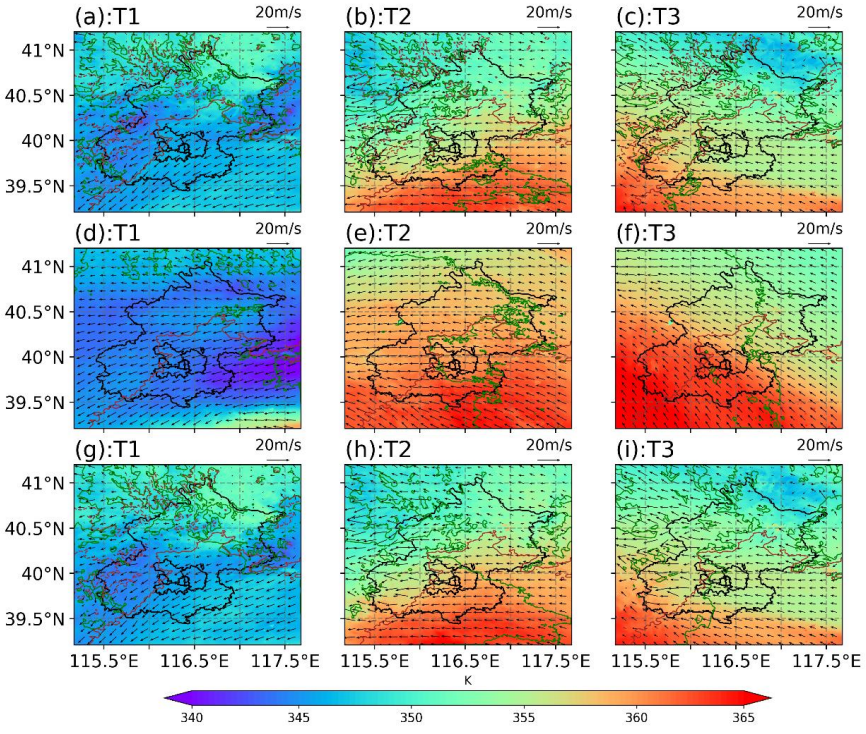

Figure 10: Simulated 2-m equivalent potential temperature, 2-m relative humidity, 10-m wind speed, and topographic height for LU_2020 scheme (a–c), LU_nohgt scheme (d–f), and LU_nourb scheme (g–i). Three consecutive time periods were selected: T1 (a, d, g), T2 (b, e, h), and T3 (c, f, i). In the figures, the 2-m temperature is represented by color-filled maps, areas with 2-m relative humidity greater than 90% are outlined by green dashed lines, the 10-m wind speed is represented by arrows, brown solid lines indicate topographic contours at 100 m, and brown dashed lines represent topographic contours at 1000 m.

The effects of topography on the wind speed, temperature, and humidity were evident (Figure 10(d–f)). During period T1, the equivalent potential temperature in the LU_2020 scheme over Beijing was significantly higher compared with that in the LU_nohgt scheme, where the largest increase was observed in the eastern and northeastern regions of Beijing. Due to the blocking effect of the mountains, the relative humidity across the entire D04 area also increased during period T1. During periods T2 and T3, the presence of the mountain range led to a notable decrease in the relative potential temperature across the region compared with the LU_nohgt scheme,

https://doi.org/10.5194/egusphere-2025-4746
Preprint. Discussion started: 21 October 2025

mainly due to the transportation of water vapor along the Taihang Mountains to the Beijing area during the second stage, where substantial amounts of water vapor and energy accumulated as the air mass passed through the mountains. The dissipation of energy and water vapor during this process led to significant reductions in the relative humidity and equivalent potential temperature in the plains and northern Beijing regions during these periods. Moreover, the presence of the western mountainous terrain led to redistribution of the water vapor, resulting in significant variability in the humidity distribution in the mountainous areas. Minimal variation was found in the overall wind direction in the plains, and there were no significant differences between the two experimental groups across all three periods. However, in the mountainous areas, the topography induced an air convergence phenomenon at the boundary between the plains and mountains. Due to the complexity of the terrain, the wind speed and direction were more heterogeneous in the western mountainous areas.

The effects of urbanization were determined between LU_2020 (Figure 10(a–c)) and LU_2020_nourb (Figure 10(g–i)). The changes were primarily concentrated in periods T2 and T3. During period T2, replacing the underlying surfaces significantly altered the 2-m relative humidity in the central urban area, with an increase of more than 5%. This increase in the relative humidity led to greater accumulation of latent heat in the air, and the 2-m equivalent potential temperature in the central urban area increased by approximately 1 K as a consequence. The wind speed increased slightly in the urban area, with greater convergence in the mountainous regions. During period T3, the increase in the relative humidity in the urban area was smaller compared with that in period T2 (around 3%). Wind speed convergence was still evident in the western mountainous regions. In particular, although the relative humidity in the central urban area increased significantly, there was no noticeable increase in the relative humidity in the downstream mountainous areas located to the east of the urban region.

3.3.3. Differences in the Vertical Profile

https://doi.org/10.5194/egusphere-2025-4746
Preprint. Discussion started: 21 October 2025

Near-surface physical quantities did not directly determine the magnitude of precipitation but alterations in the underlying surface could be manifest in changes in the near-surface physical quantities, which subsequently influenced the upper atmosphere and affected the intensity of precipitation. Thus, the mechanisms that allowed surface modifications to affect the overall precipitation event were elucidated by examining the influence of underlying surface changes on upper-level precipitation-related physical variables. We explored the mechanisms associated with variations in precipitation by comparative analysis of the meridional and zonal vertical profiles. Figure 11 presents the meridional and zonal vertical profiles for the three distinct time periods.

In the LU_2020 scheme, during period T1, convection was primarily confined to the mountainous regions and the plains to the east of the mountains. The topographic blocking effect resulted in significant upward motion in both the mountainous areas and adjacent plains. Around 02:00 on July 30, the eastward water vapor flux was sufficiently high during period T1, leading to condensation of substantial amounts of water vapor into cloud and raindrop particles over the mountainous regions. The latent heat released in this process induced fluctuations in the equivalent potential temperature contours in the upper levels. In the zonal direction, cloud and raindrop particles were predominantly located over the southern mountains. In the northern mountainous areas, due to the relatively low water vapor flux and lower equivalent potential temperature, there was almost no vertical motion in the air, resulting in negligible cloud droplet formation in this region.

During period T2, the atmosphere over the mountainous regions was characterized by vigorous convection in the meridional direction. In the southwestern mountains, higher equivalent potential temperatures correlated with greater cloud droplet contents. Both the southerly winds and vertical wind speeds increased significantly compared with period T1, and the cloud water and rainwater mixing ratios were elevated near 39.8 °N. The cloud water mixing ratios were relatively high in other regions but this corresponded to the early stages of precipitation when cloud

https://doi.org/10.5194/egusphere-2025-4746
Preprint. Discussion started: 21 October 2025

water had yet to fully transition into rainwater, resulting in low rainwater contents in most areas.

In the meridional direction, only the low-level wind speed over the plains was noticeably higher in period T3. The low-level winds exhibited convergence, whereas the upper-level winds exhibited divergence in the southwestern mountainous region, and thus the equivalent potential temperature remained relatively high near the surface. In the zonal direction, notable convection occurred over the mountainous areas, accompanied by significant fluctuations in the near-surface potential temperature. In addition, during this period, the southward water vapor flux was relatively large, and the energy, water vapor, and motion within the southwestern mountainous regions were conducive to the development of convection. As illustrated in Figure 11(i–k), marked increases occurred in both the cloud water and rainwater contents in the southwestern mountainous area compared with other regions. Consequently, this region experienced relatively higher precipitation during period T3.

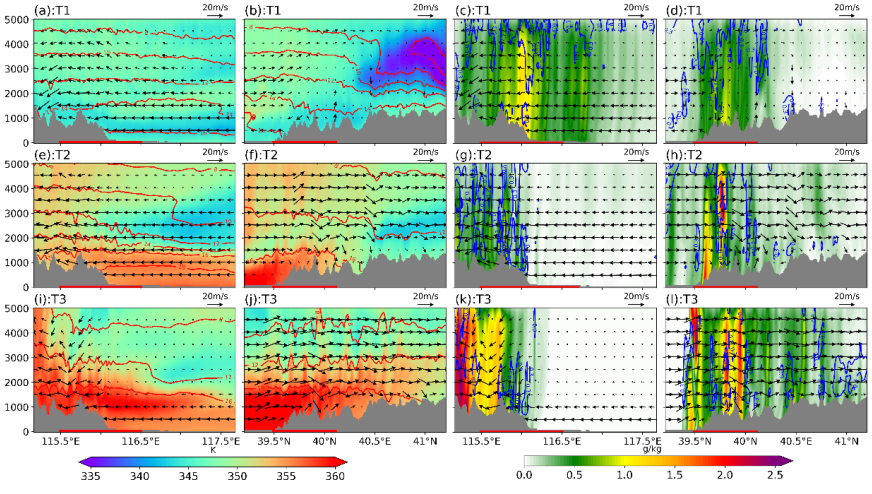

Figure 11: Meridional-vertical profiles (a, c, e, g, i, k) at 39.9 ℃N and zonal-vertical profiles (b, d, f, h, j, l) at 115.7 ℃E for LU_2020. In (a, b, e, f, i, j), the shaded areas represent the magnitude of the equivalent potential temperature and red contours indicate the water vapor mixing ratio. In panels (c, d, g, h, k, l), the shaded areas represent the rainwater mixing ratio and blue contours indicate the cloud water mixing ratio. The arrows represent the horizontal wind vectors (with the vertical wind speed amplified by a factor of five). Gray shading denotes the terrain height. The red line at the bottom of the map indicates region RegP, as shown in Figure 6.

https://doi.org/10.5194/egusphere-2025-4746
Preprint. Discussion started: 21 October 2025

Comparisons between the LU_2020 (Figure 11(a–l)) and LU_nohgt (Figure 12(a1–l1)) experimental groups highlighted the convection observed during periods driven by orographic uplift. In period T1, the uplift motion in the southern part of the area facilitated the condensation of cloud and raindrop particles, and thus the precipitation intensity increased. In period T2, due to the higher equivalent potential temperature and water vapor content of the atmosphere, strong convection persisted in the western part of the area in LU_nohgt. The intensity of convection and water droplet concentration in the atmosphere were markedly higher than those observed in the LU_2020 scheme. In the zonal direction, significant differences were observed between the locations of cloud water particle accumulation under the two experimental setups. In period T3, convection shifted northward with the southerly winds in the LU_nohgt scheme. At the southern edge of the convective cloud mass, the distributions of the wind speed, temperature, and humidity stabilized, indicating the cessation of intense precipitation in the region. Despite the high energy levels within the study area, the absence of orographic uplift led to a reduction in the intensity of precipitation, and the precipitation event ended earlier compared with the LU_2020 scheme.

The impacts of urbanization on precipitation outcomes were examined by comparing the LU_2020 (Figure 11(a–l)) and LU_nourb (Figure 12(a2–l2)) schemes, where the primary effects were observed during periods T2 and T3. Due to the influence of urbanization, no significant change in the cloud water content occurred over the mountainous areas during period T2, but the rainwater content was markedly reduced, indicating a smaller amount of precipitation relative to LU_nourb. Urbanization led to decreases in the water vapor and energy transported into the mountains from the eastern and southern parts of the region, thereby reducing the condensation of cloud water and water vapor particles, which also agreed with the delayed precipitation observed in the second period due to urbanization. During period T3, both the meridional and zonal convection activities were weaker compared with LU_nourb, and the locations of cloud droplet particles were also altered. In

https://doi.org/10.5194/egusphere-2025-4746
Preprint. Discussion started: 21 October 2025

summary, during periods T2 and T3, the predominant near-surface wind direction in the central urban area was an easterly flow. The presence of the city reduced the latent heat flux in the region, thereby diminishing the amount of energy transported into the southwestern mountainous areas, and thus intense precipitation occurred in the southwestern mountainous region during periods T2 to T3.

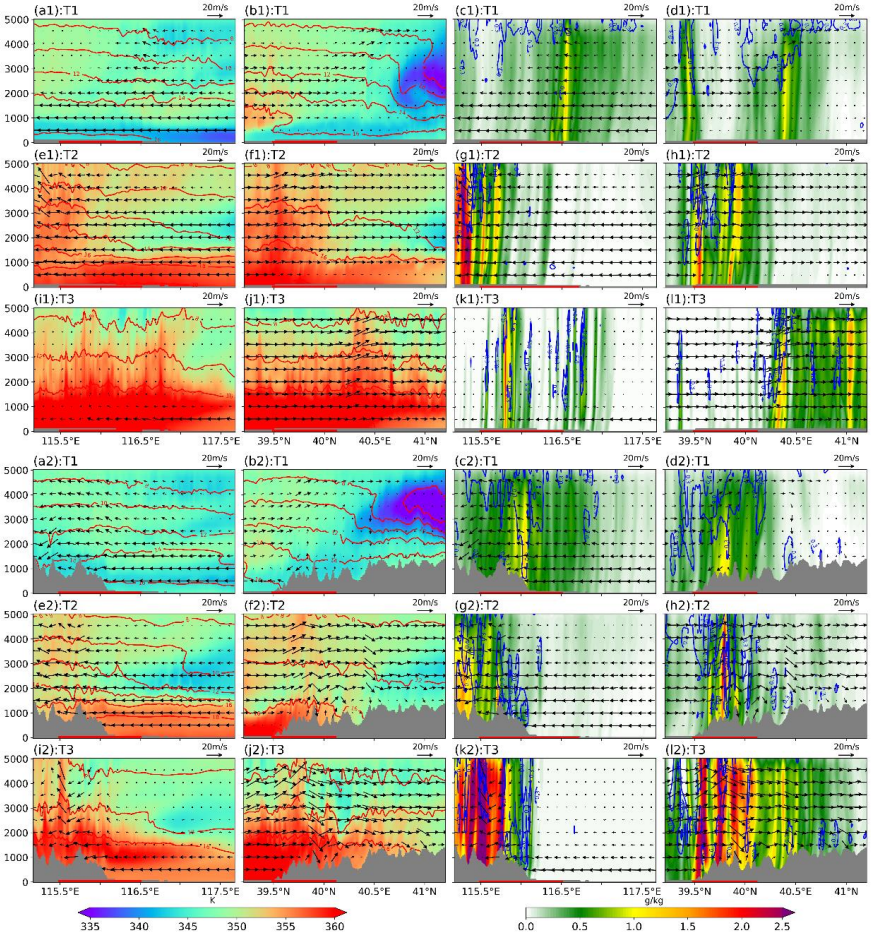

Figure 12: Meridional-vertical and zonal-vertical profiles for the LU_nohgt and LU_nourb schemes. The physical quantities are consistent with those shown in Figure 11. Panels (a1–l1) represent the meridional-vertical and zonal-vertical profiles for the LU_nohgt scheme, and panels (a2–l2) represent the meridional-vertical and zonal-vertical profiles for the LU_nourb scheme.

4. Discussion

https://doi.org/10.5194/egusphere-2025-4746
Preprint. Discussion started: 21 October 2025

In present study, simulations were conducted using the WRF model to investigate the changes in the timing and spatial distribution of precipitation during the "7 31" event caused by the effects of topographic and urban land use. Previous studies have also analyzed the mechanisms related to precipitation and the impacts of topography on extreme precipitation events (Gao et al., 2024; Li et al., 2024b). In contrast to previous analyses, we explored the effects of mountain-plain topographic conditions by altering the underlying surfaces as well as investigating the impact of urbanization on this extreme precipitation event. We identified the primary causes of this extreme precipitation event by considering three time periods with significant differences in precipitation and analyzing the changes in basic physical quantities.

Our findings served as an extension and complement to previous experiments. Due to the lack of observational data from stations, we were unable to accurately capture the development of the entire precipitation event. However, our simulations results were generally consistent with those obtained by CMORPH, suggesting that the mechanisms identified by the model are relatively reliable. According to previous studies, the impacts of topography on short-duration extreme precipitation events have not been thoroughly explored using the currently available simulation models (O'Gorman, 2015), thereby suggesting that it is still possible to improve the accuracy of precipitation simulations in numerical models for regions with complex terrain.

Previous studies have pointed out that regional climate models have some limits on reproducing large-scale circulation features (Kukulies et al., 2023; Yu et al., 2024). To address this limitation, the spectral nudging was applied to the D01 domain in all schemes. The ERA5 reanalysis data was used to constrain large-scale circulation of the model, while allowing freely development for mesoscale and small-scale processes within the domain (Ma et al., 2022; Miguez-Macho et al., 2005; von Storch et al., 2000; Waldron et al., 1996). Therefore, it can provide a more accurate large-scale flow fields to the inner domains. The simulation results showed that, the orography and land use modifications in this study primarily influenced local circulation patterns and had limited impact on synoptic-scale weather systems.

https://doi.org/10.5194/egusphere-2025-4746
Preprint. Discussion started: 21 October 2025

Previous studies also found that, the modifications of local urban land surface can influence local-scale atmospheric circulation (Kim et al., 2021; Sui et al., 2024; Zajic et al., 2011). The widespread presence of impervious surfaces in urban areas restrained surface evaporation, by reducing the upward transport of moisture into the atmosphere. This process can lead to low relative humidity and reduce atmospheric instability, which in turn modifies the local precipitation distribution (Wang et al., 2018).

According to previous research, the maximum reduction in precipitation due to urbanization during warm-season rainfall occurs in the northeastern region of Beijing (Song et al., 2014; Wang et al., 2018). However, in the present study, the largest reduction in precipitation induced by urbanization was observed in the southwestern mountainous region. The main causes of this anomalous precipitation distribution were attributed to the orographic effects of the Taihang and Yanshan Mountains. In our experiment that considered urban land use types without accounting for topographic height, we found that the increases in the accumulated precipitation and average precipitation intensity in the southwestern mountainous region were significantly reduced, whereas increases were simulated in most areas of northern Beijing area. Therefore, compared with the changes in the average distribution of seasonal precipitation in Beijing found in previous studies, individual case experiments may simulate precipitation distribution patterns that differ from the multi-year observed accumulated precipitation. In the present study, the orographic lifting effect of the terrain was undoubtedly the main factor that influenced the extreme precipitation event.

The concentrations of aerosols emitted in urban areas could also have influenced the amount of precipitation in this event because precipitation formation is largely driven by the coalescence of cloud droplets. Studies have shown that aerosols can lead to the formation of smaller-sized cloud droplets, increasing the effective radius of precipitation, and thus impact convective rainfall (Sun et al., 2022; Zhong et al., 2015). In addition, topographic variations can affect the generation of cloud particles (Lee et

https://doi.org/10.5194/egusphere-2025-4746
Preprint. Discussion started: 21 October 2025

al., 2018; Mazzetti et al., 2021). Therefore, the impacts of aerosols on this precipitation event should be investigated in future research.

In this study, we conducted simulations using selected parameterization schemes and analyzed their impacts on the underlying surface. However, the high computational costs associated with high-resolution numerical simulations prevented us from performing an ensemble simulation of the entire precipitation event, which may have introduced uncertainty into the simulation results. Further analyses of the precipitation mechanisms were also hindered due to the limited availability of observational data from mountainous stations and the inability of some meteorological stations to accurately transmit real-time precipitation data because of the influence of precipitation.

5. Conclusion

In this study, we used the WRF model to analyze the extreme precipitation event that occurred in the Beijing region from July 29 to August 2, 2023. The effects of topography and land use on the precipitation process were evaluated by removing the topography and replacing urban land use types with croplands from the updated land use experiment group. The results showed that, the areas influenced most significantly by topography were concentrated in the southwestern mountainous region of Beijing. Presence of terrain caused orographic uplift and increased the precipitation within the mountainous area by more than 40% during the event. This main because that the mountainous area blocked the existence of the low-pressure system of typhoon Doksuri from propagating northward and lead to extended duration of the precipitation event by approximately 12 h. The underlying urban surfaces also altered the overall precipitation process. For the scheme removing the underlying urban surfaces the enhanced water vapor flux transported by low-level easterly winds to the southwestern mountainous region of the city increased the accumulation of energy and water vapor in the region. After July 31, the accumulation of sufficient energy and moisture in the southwestern mountainous region strengthened the intensity of

https://doi.org/10.5194/egusphere-2025-4746
Preprint. Discussion started: 21 October 2025

precipitation. In addition, removing the underlying urban surface caused an increase in the wind speed in the plain areas, which led to large convergence at the mountain boundary and contributed to stronger precipitation. These findings can help us with the prevention and response to similar future events, and possibly reduce the likelihood of disasters.

Financial Support

This study was funded by the National Natural Science Foundation of China (42077421 and 41930970).

Data Availability Statement

The ERA5 reanalysis data can be downloaded at Climate Data Store (https://cds.climate.copernicus.eu). The CMOPRH precipitation data were obtained from Climate Prediction Center. (https://www.ncei.noaa.gov/products/climate-data-records/precipitation-cmorph). The updated land use/land cover data from MCD12Q1 V6 over Beijing region are available from the Land Processes Distributed Active Archive Center (https://lpdaac.usgs.gov/).

Author Contributions

Haobo Cui: Conceptualization; formal analysis; methodology; software; validation; visualization; writing – original draft; writing – review and editing. **Hongyong Yu**: Conceptualization; methodology; writing – review and editing. **Xingshuo Zuo**: methodology; writing – review and editing. **Guocan Wu**: Conceptualization; data curation; funding acquisition; investigation resources; supervision; writing – original draft; writing – review and editing.

Conflicts of Interest

The authors declare that they have no conflict of interest.

https://doi.org/10.5194/egusphere-2025-4746
Preprint. Discussion started: 21 October 2025

References

1. Ayat, H., J. P. Evans, S. C. Sherwood, and J. Soderholm, 2022: Intensification of subhourly heavy rainfall. *Science*, **378,** 655-+.
2. Bhattarai, S., and R. Talchabhadel, 2024: Comparative Analysis of Satellite-Based Precipitation Data across the CONUS and Hawaii: Identifying Optimal Satellite Performance. *Remote Sensing*, **16**, 3058.
3. Bornstein, R., and Q. L. Lin, 2000: Urban heat islands and summertime convective thunderstorms in Atlanta: three case studies. *Atmospheric Environment*, **34,** 507-516.
4. Chen, F., and J. Dudhia, 2001: Coupling an advanced land surface-hydrology model with the Penn State-NCAR MM5 modeling system. Part II: Preliminary model validation. *Monthly Weather Review*, **129,** 587-604.
5. Chen, F., H. Kusaka, R. Bornstein, J. Ching, C. S. B. Grimmond, S. Grossman-Clarke, T. Loridan, K. W. Manning, A. Martilli, S. G. Miao, D. Sailor, F. P. Salamanca, H. Taha, M. Tewari, X. M. Wang, A. A. Wyszogrodzki, and C. L. Zhang, 2011: The integrated WRF/urban modelling system: development, evaluation, and applications to urban environmental problems. *International Journal of Climatology*, **31,** 273-288.
6. Chen, M. X., Y. C. Wang, F. Gao, and X. Xiao, 2014: Diurnal evolution and distribution of warm-season convective storms in different prevailing wind regimes over contiguous North China. *Journal of Geophysical Research-Atmospheres*, **119,** 2742-2763.
7. Cornejo, I. C., A. K. Rowel, K. L. Rasmussen, and J. C. Dehartb, 2024: Orographic Controls on Extreme Precipitation Associated with a Mei-Yu Front. *Monthly Weather Review*, **152,** 531-551.
8. Dai, P. X., J. Nie, Y. Yu, and R. G. Wu, 2024: Constraints on regional projections of mean and extreme precipitation under warming. *Proceedings of the National Academy of Sciences of the United States of America*, **121**.
9. Davolio, S., A. Buzzi, and P. Malguzzi, 2009: Orographic triggering of long lived convection in three dimensions. *Meteorology and Atmospheric Physics*, **103,** 35-44.
10. Dixon, P. G., and T. L. Mote, 2003: Patterns and causes of Atlanta's urban heat island-initiated precipitation. *Journal of Applied Meteorology*, **42,** 1273-1284.
11. Du, Y., G. X. Chen, B. Han, L. Q. Bai, and M. H. Li, 2020: Convection Initiation and Growth at the Coast of South China. Part II: Effects of the Terrain, Coastline, and Cold Pools. *Monthly Weather Review*, **148,** 3871-3892.
12. Dudhia, J., 1989: Numerical Study of Convection Observed during the Winter Monsoon Experiment Using a Mesoscale Two-Dimensional Model. *Journal of the Atmospheric Sciences*, **46,** 3077-3107.
13. Ebert, E. E., J. E. Janowiak, and C. Kidd, 2007: Comparison of near-real-time precipitation estimates from satellite observations and numerical models. *Bulletin of the American Meteorological Society*, **88**, 47-64.
14. Feddema, J. J., K. W. Oleson, G. B. Bonan, L. O. Mearns, L. E. Buja, G. A. Meehl, and W. M. Washington, 2005: The importance of land-cover change in simulating future climates. *Science*, **310,** 1674-1678.
15. Freitag, B. M., U. S. Nair, and D. Niyogi, 2018: Urban Modification of Convection and Rainfall in Complex Terrain. *Geophysical Research Letters*, **45,** 2507-2515.
16. Friedl, M., D. Sulla-Menashe, 2019: MCD12Q1 MODIS/Terra+Aqua Land Cover Type Yearly L3 Global 500m SIN Grid V006. *NASA EOSDIS Land Processes Distributed Active Archive*

https://doi.org/10.5194/egusphere-2025-4746
Preprint. Discussion started: 21 October 2025

Center.

17. Fu, Y. Y., Y. A. Mao, and G. C. Wu, 2024a: Event-based evaluation of urbanization impact on precipitation during the 1978-2021 warm season over eastern China. *Urban Climate*, **56**.
18. Gao, X. Y., J. S. Sun, J. F. Yin, A. Abulikemu, C. Wu, X. D. Liang, and R. D. Xia, 2024: The impact of mountain-plain thermal contrast on precipitation distributions during the "23.7" record-breaking heavy rainfall over North China. *Atmospheric Research*, **310**.
19. Gao, Y. H., F. Chen, M. Barlage, W. Liu, G. D. Cheng, X. Li, Y. Yu, Y. H. Ran, H. Y. Li, H. C. Peng, and M. G. Ma, 2008: Enhancement of land surface information and its impact on atmospheric modeling in the Heihe River Basin, northwest China. *Journal of Geophysical Research-Atmospheres*, **113**.
20. Gao, Z. B., J. S. Zhu, Y. Guo, N. Luo, Y. Fu, and T. T. Wang, 2021: Impact of Land Surface Processes on a Record-Breaking Rainfall Event on May 06-07, 2017, in Guangzhou, China. *Journal of Geophysical Research-Atmospheres*, **126**.
21. Gimeno, L., A. Drumond, R. Nieto, R. M. Trigo, and A. Stohl, 2010: On the origin of continental precipitation. *Geophysical Research Letters*, **37**.
22. He, H. Z., and F. Q. Zhang, 2010: Diurnal Variations of Warm-Season Precipitation over Northern China. *Monthly Weather Review*, **138,** 1017-1025.
23. Hersbach, H., B. Bell, P. Berrisford, S. Hirahara, A. Horányi, J. Muñoz-Sabater, J. Nicolas, C. Peubey, R. Radu, D. Schepers, A. Simmons, C. Soci, S. Abdalla, X. Abellan, G. Balsamo, P. Bechtold, G. Biavati, J. Bidlot, M. Bonavita, G. De Chiara, P. Dahlgren, D. Dee, M. Diamantakis, R. Dragani, J. Flemming, R. Forbes, M. Fuentes, A. Geer, L. Haimberger, S. Healy, R. J. Hogan, E. Hólm, M. Janisková, S. Keeley, P. Laloyaux, P. Lopez, C. Lupu, G. Radnoti, P. de Rosnay, I. Rozum, F. Vamborg, S. Villaume, and J. N. Thépaut, 2020: The ERA5 global reanalysis. *Quarterly Journal of the Royal Meteorological Society*, **146,** 1999-2049.
24. Hjelmfelt, M. R., 1982: Numerical Simulation of the Effects of St. Louis on Mesoscale Boundary-Layer Airflow and Vertical Air Motion: Simulations of Urban vs Non-Urban Effects. *Journal of Applied Meteorology*, **21,** 1239-1257.
25. Holst, C. C., C. Y. Tam, and J. C. L. Chan, 2016: Sensitivity of urban rainfall to anthropogenic heat flux: A numerical experiment. *Geophysical Research Letters*, **43,** 2240-2248.
26. Hong, S. Y., Y. Noh, and J. Dudhia, 2006: A new vertical diffusion package with an explicit treatment of entrainment processes. *Monthly Weather Review*, **134,** 2318-2341.
27. Hong, S. Y., and J.–O. J. Lim, 2006: The WRF single–moment 6–class microphysics scheme (WSM6). *Journal of the Korean Meteorological Society*, **42,** 129-151.
28. IPCC, 2021: *The Physical Science Basis. Contribution of Working Group I to the Sixth Assessment Report of the Intergovernmental Panel on Climate Change.* Cambridge University Press.
29. Jauregui, E., and E. Romales, 1996: Urban effects on convective precipitation in Mexico city. *Atmospheric Environment*, **30,** 3383-3389.
30. Jiang, S.-h., M. Zhou, L.-l. Ren, X.-r. Cheng, and P.-j. Zhang, 2016: Evaluation of latest TMPA and CMORPH satellite precipitation products over Yellow River Basin. *Water Science and Engineering*, **9**, 87-96.
31. Jiménez, P. A., J. Dudhia, J. F. González-Rouco, J. Navarro, J. P. Montávez, and E. García-Bustamante, 2012: A Revised Scheme for the WRF Surface Layer Formulation. *Monthly Weather Review*, **140,** 898-918.

https://doi.org/10.5194/egusphere-2025-4746
Preprint. Discussion started: 21 October 2025

32. Joyce, R. J., J. E. Janowiak, P. A. Arkin, and P. P. Xie, 2004: CMORPH: A method that produces global precipitation estimates from passive microwave and infrared data at high spatial and temporal resolution. *Journal of Hydrometeorology*, **5,** 487-503.
33. Kain, J. S., 2004: The Kain-Fritsch convective parameterization: An update. *Journal of Applied Meteorology*, **43,** 170-181.
34. Kim, G., J. Lee, M.-I. Lee, and D. Kim, 2021: Impacts of urbanization on atmospheric circulation and aerosol transport in a coastal environment simulated by the WRF-Chem coupled with urban canopy model. *Atmospheric Environment*, **249,** 118253.
35. Krakauer, N. Y., S. M. Pradhanag, T. Lakhankar, and A. K. Jha, 2013: Evaluating Satellite Products for Precipitation Estimation in Mountain Regions: A Case Study for Nepal. *Remote Sensing*, **5,** 4107-4123.
36. Lee, J. T., K. Y. Ko, D. I. Lee, C. H. You, and Y. C. Liou, 2018: Enhancement of orographic precipitation in Jeju Island during the passage of Typhoon Khanun (2012). *Atmospheric Research*, **201,** 58-71.
37. Li, S., Y. N. Chen, W. Wei, G. H. Fang, and W. L. Duan, 2024a: The increase in extreme precipitation and its proportion over global land. *Journal of Hydrology*, **628**.
38. Li, W. B., S. Chen, G. X. Chen, W. M. Sha, C. Luo, Y. R. Feng, Z. P. Wen, and B. M. Wang, 2011: Urbanization signatures in strong versus weak precipitation over the Pearl River Delta metropolitan regions of China. *Environmental Research Letters*, **6**.
39. Li, X., S. W. Zhao, and D. H. Wang, 2024b: Roles of synoptic characteristics and microphysics processes on the heavy rain event over Beijing region during 29 July to 2 August 2023. *Frontiers in Earth Science*, **12**, 1394342.
40. Lin, Y. L., S. Chiao, T. A. Wang, M. L. Kaplan, and R. P. Weglarz, 2001: Some common ingredients for heavy orographic rainfall. *Weather and Forecasting*, **16,** 633-660.
41. Liu, S., J. Wang, and H. Wang, 2022: Assessing 10 Satellite Precipitation Products in Capturing the July 2021 Extreme Heavy Rain in Henan, China. *Journal of Meteorological Research*, **36**, 798-808.
42. Lu, X. Y., G. Q. Tang, X. Q. Wang, Y. Liu, L. H. Jia, G. H. Xie, S. Li, and Y. X. Zhang, 2019: Correcting GPM IMERG precipitation data over the Tianshan Mountains in China. *Journal of Hydrology*, **575,** 1239-1252.
43. Ma, M., P. Hui, D. Liu, P. Zhou, and J. Tang, 2022: Convection-permitting regional climate simulations over Tibetan Plateau: re-initialization versus spectral nudging. *Climate Dynamics*, **58,** 1719-1735.
44. Mahoney, K. M., 2016: The Representation of Cumulus Convection in High-Resolution Simulations of the 2013 Colorado Front Range Flood. *Monthly Weather Review*, **144,** 4265-4278.
45. Mazzetti, T. O., B. Geerts, L. L. Xue, S. Tessendorf, C. Weeks, and Y. G. Wang, 2021: Potential for Ground-Based Glaciogenic Cloud Seeding over Mountains in the Interior Western United States and Anticipated Changes in a Warmer Climate. *Journal of Applied Meteorology and Climatology*, **60,** 1245-1263.
46. Miguez-Macho, G., G. L. Stenchikov, and A. Robock, 2004: Spectral nudging to eliminate the effects of domain position and geometry in regional climate model simulations. *Journal of Geophysical Research-Atmospheres*, **109**.
47. Mlawer, E. J., S. J. Taubman, P. D. Brown, M. J. Iacono, and S. A. Clough, 1997: Radiative transfer for inhomogeneous atmospheres: RRTM, a validated correlated-k model for the

https://doi.org/10.5194/egusphere-2025-4746
Preprint. Discussion started: 21 October 2025

longwave. *Journal of Geophysical Research-Atmospheres*, **102,** 16663-16682.

48. Nicolas, Q., and W. R. Boos, 2024: Understanding the Spatiotemporal Variability of Tropical Orographic Rainfall Using Convective Plume Buoyancy. *Journal of Climate*, **37,** 1737-1757.
49. Nie, W. S., B. F. Zaitchik, G. H. Ni, and T. Sun, 2017: Impacts of Anthropogenic Heat on Summertime Rainfall in Beijing. *Journal of Hydrometeorology*, **18,** 693-712.
50. Oke, T. R., 1982: The energetic basis of the urban heat island. *Quarterly Journal of the Royal Meteorological Society*, **108,** 1-24.
51. Pendergrass, A. G., and R. Knutti, 2018: The Uneven Nature of Daily Precipitation and Its Change. *Geophysical Research Letters*, **45,** 11980-11988.
52. Saurral RI, Camilloni IA, Ambrizzi T, 2015: Links between topography, moisture fluxes pathways and precipitation over South America. Clim Dyn 45(3):777–789
53. Shen, Y., A. Y. Xiong, Y. Wang, and P. P. Xie, 2010: Performance of high-resolution satellite precipitation products over China. *Journal of Geophysical Research-Atmospheres*, **115**.
54. Skamarock, W. C., J. B. Klemp, J. Dudhia, D. O. Gill, Z. Liu, J. Berner, W. Wang, J. G. Powers, M. G. Duda, D. M. Barker, and X.-Y. Huang, 2019: A Description of the Advanced Research WRF Version 4. *NCAR Tech. Note NCAR/TN-556+STR*, **145 pp**.
55. Smith, R. B., 2006: Progress on the theory of orographic precipitation. *Tectonics, Climate, and Landscape Evolution*, 1-16.
56. Song, X. M., J. Y. Zhang, A. AghaKouchak, S. Sen Roy, Y. Q. Xuan, G. Q. Wang, R. M. He, X. J. Wang, and C. S. Liu, 2014: Rapid urbanization and changes in spatiotemporal characteristics of precipitation in Beijing metropolitan area. *Journal of Geophysical Research-Atmospheres*, **119,** 11250-11271.
57. Spero, T. L., M. J. Otte, J. H. Bowden, and C. G. Nolte, 2014: Improving the representation of clouds, radiation, and precipitation using spectral nudging in the Weather Research and Forecasting model. *Journal of Geophysical Research-Atmospheres*, **119,** 11682-11694.
58. Sui, X., Z.-L. Yang, M. Shepherd, and D. Niyogi, 2024: Global scale assessment of urban precipitation anomalies. *Proceedings of the National Academy of Sciences*, **121,** e2311496121.
59. Sun, N., Y. F. Fu, L. Zhong, and R. Li, 2022: Aerosol effects on the vertical structure of precipitation in East China. *NPJ Climate and Atmospheric Science*, **5**.
60. Sun, Q. H., X. B. Zhang, F. Zwiers, S. Westra, and L. Alexander, 2021: A Global, Continental, and Regional Analysis of Changes in Extreme Precipitation. *Journal of Climate*, **34,** 243-258.
61. Sun, R., H. Yuan, X. Liu, and X. Jiang, 2016: Evaluation of the latest satellite–gauge precipitation products and their hydrologic applications over the Huaihe River basin. *Journal of Hydrology*, **536**, 302-319.
62. Tewari, M., F. Chen, J. Dudhia, P. Ray, S. G. Miao, E. Nikolopoulos, and L. Treinish, 2022: Understanding the sensitivity of WRF hindcast of Beijing extreme rainfall of 21 July 2012 to microphysics and model initial time. *Atmospheric Research*, **271**.
63. Tewari, M., F. Chen, W. Wang, J. Dudhia, M. A. LeMone, K. Mitchell, M. Ek, G. Gayno, J. Wegiel, and R. H. Cuenca, 2004: Implementation and verification of the unified NOAH land surface model in the WRF model. *20th conference on weather analysis and forecasting/16th conference on numerical weather prediction*.
64. Trenberth, K. E., A. Dai, R. M. Rasmussen, and D. B. Parsons, 2003: The changing character of precipitation. *Bulletin of the American Meteorological Society*, **84,** 1205-1217.
65. von Storch, H., H. Langenberg, and F. Feser, 2000: A Spectral Nudging Technique for Dynamical

https://doi.org/10.5194/egusphere-2025-4746
Preprint. Discussion started: 21 October 2025

Downscaling Purposes. *Monthly Weather Review*, **128,** 3664-3673.

66. Waldron, K. M., J. Paegle, and J. D. Horel, 1996: Sensitivity of a Spectrally Filtered and Nudged Limited-Area Model to Outer Model Options. *Monthly Weather Review*, **124,** 529-547.
67. Wang, H. C., and Z. Zhong, 2014: Ensemble simulations to investigate the impact of large-scale urbanization on precipitation in the lower reaches of Yangtze River Valley, China. *Quarterly Journal of the Royal Meteorological Society*, **140,** 258-266.
68. Wang, J., J. M. Feng, and Z. W. Yan, 2015: Potential sensitivity of warm season precipitation to urbanization extents: Modeling study in Beijing-Tianjin-Hebei urban agglomeration in China. *Journal of Geophysical Research-Atmospheres*, **120,** 9408-9425.
69. ——, 2018: Impact of Extensive Urbanization on Summertime Rainfall in the Beijing Region and the Role of Local Precipitation Recycling. *Journal of Geophysical Research-Atmospheres*, **123,** 3323-3340.
70. Wang, X. Q., and Y. B. Gong, 2010: The impact of an urban dry island on the summer heat wave and sultry weather in Beijing City. *Chinese Science Bulletin*, **55,** 1657-1661.
71. Wei, P., X. Xu, M. Xue, C. Y. Zhang, Y. Wang, K. Zhao, A. Zhou, S. S. Zhang, and K. F. Zhu, 2023: On the Key Dynamical Processes Supporting the 21.7 Zhengzhou Record-breaking Hourly Rainfall in China. *Advances in Atmospheric Sciences*, **40,** 337-349.
72. Wu, G. C., Y. Li, S. Qin, Y. N. Mao, and K. C. Wang, 2021: Precipitation Unevenness in Gauge Observations and Eight Reanalyses from 1979 to 2018 over China. *Journal of Climate*, **34,** 9797-9810.
73. Xia, R. D., and D. L. Zhang, 2019: An Observational Analysis of Three Extreme Rainfall Episodes of 19-20 July 2016 along the Taihang Mountains in North China. *Monthly Weather Review*, **147,** 4199-4220.
74. Yan, L., D. Lu, L. Xiong, H. Wang, Q. Luan, C. Jiang, B. Xiong, W. Xu, P. Yan, Q. Lei, and C. Y. Xu, 2023: Derivation of nonstationary rainfall intensity-duration-frequency curves considering the impacts of climate change and urbanization. *Urban Climate*, **52**.
75. Yang, P., G. Y. Ren, and P. C. Yan, 2017: Evidence for a Strong Association of Short-Duration Intense Rainfall with Urbanization in the Beijing Urban Area. *Journal of Climate*, **30,** 5851-5870.
76. Yin, J. F., D. L. Zhang, Y. L. Luo, and R. Y. Ma, 2020: On the Extreme Rainfall Event of 7 May 2017 over the Coastal City of Guangzhou. Part I: Impacts of Urbanization and Orography. *Monthly Weather Review*, **148,** 955-979.
77. Yu, H. Y., A. F. Prein, D. Qi, and K. C. Wang, 2024: Kilometer-scale multi-physics simulations of heavy precipitation events in Northeast China. *Climate Dynamics*, **62,** 9207-9231.
78. Yu, M., and Y. M. Liu, 2015: The possible impact of urbanization on a heavy rainfall event in Beijing. *Journal of Geophysical Research-Atmospheres*, **120,** 8132-8143.
79. Yu, M., S. G. Miao, and Q. C. Li, 2017: Synoptic analysis and urban signatures of a heavy rainfall on 7 August 2015 in Beijing. *Journal of Geophysical Research-Atmospheres*, **122,** 65-78.
80. Zajic, D., H. J. S. Fernando, R. Calhoun, M. Princevac, M. J. Brown, and E. R. Pardyjak, 2011: Flow and Turbulence in an Urban Canyon. *Journal of Applied Meteorology and Climatology*, **50,** 203-223.
81. Zhang, D. L., Y. H. Lin, P. Zhao, X. D. Yu, S. Q. Wang, H. W. Kang, and Y. H. Ding, 2013: The Beijing extreme rainfall of 21 July 2012: "Right results" but for wrong reasons. *Geophysical Research Letters*, **40**.
82. Zhang, W. X., K. Furtado, T. J. Zhou, P. L. Wu, and X. L. Chen, 2022: Constraining extreme

https://doi.org/10.5194/egusphere-2025-4746
Preprint. Discussion started: 21 October 2025

precipitation projections using past precipitation variability. *Nature Communications*, **13**.

83. Zhang, Y. Z., S. G. Miao, Y. J. Dai, and R. Bornstein, 2017: Numerical simulation of urban land surface effects on summer convective rainfall under different UHI intensity in Beijing. *Journal of Geophysical Research-Atmospheres*, **122,** 7851-7868.
84. Zhao, D. M., B. K. Su, and M. Zhao, 2006: Soil moisture retrieval from satellite images and its application to heavy rainfall simulation in eastern China. *Advances in Atmospheric Sciences*, **23,** 299-316.
85. Zhong, S., Y. Qian, C. Zhao, R. Leung, and X. Q. Yang, 2015: A case study of urbanization impact on summer precipitation in the Greater Beijing Metropolitan Area: Urban heat island versus aerosol effects. *Journal of Geophysical Research-Atmospheres*, **120,** 10903-10914.